Catalysis Today 161 (2011) 8–14

Contents lists available at ScienceDirect

Catalysis Today

journal homepage: www.elsevier.com/locate/cattod

Photoelectrochemical properties of hierarchical nanocomposite structure: Carbon nanofibers/TiO_2/ZnO thin films

S. Kment[a,*], Z. Hubicka[a], H. Kmentova[b], P. Kluson[b], J. Krysa[b], I. Gregora[a], M. Morozova[b], M. Cada[a], D. Petras[b], P. Dytrych[a], M. Slater[c], L. Jastrabik[a]

[a] Institute of Physics, Academy of Sciences of the Czech Republic, Na Slovance 2, 182 21 Prague 8, Czech Republic
[b] Institute of Chemical Process Fundamentals, Academy of Sciences of the Czech Republic, Rozvojova 135, 165 02 Prague 6, Czech Republic
[c] The School of Chemistry, Bangor University, Bangor, Gwynedd LL57 2UW, UK

ARTICLE INFO

Article history:
Available online 3 November 2010

Keywords:
Thin layers
Hollow cathode
TiO_2
ZnO
CNFs
IPCE
Photocatalysis

ABSTRACT

The basic objective of this work is related to the research on the design of hierarchic multilayer systems with the assumed final functionality utilized for microelectronics and photovoltaics. We report on photoelectrochemical functionality of the multilayer system consisting of carbon nanofibers (CNFs)/photoactive anatase TiO_2/conductive ZnO thin films. The CNFs' layers were obtained by annealing the polyacrylonitrile (PAN) web deposited by the electrospinning method. Titanium dioxide and zinc oxide layers were deposited by means of a hollow cathode cold plasma deposition system. Raman spectra confirmed carbon nanofibers, crystalline TiO_2 and ZnO forming individual layers as well as the final multilayer assembly. A mixture of various $Zn_xTi_yO_z$ phases was also observed. These structures were produced due to the reactions between the highly energetic zinc ions generated in the plasma environment and the TiO_2 layer. The same phenomenon is probably responsible for the doping of TiO_2 by carbon atoms originating from CNFs and leading to a significant decrease of the photocatalytic activity.

1. Introduction

There have been significant advances in the development of heterogeneous photocatalysts based on metal oxide semiconductor thin films, mostly of anatase TiO_2 [1–7]. Also ZnO possesses high photocatalytic efficiency but it holds the drawback of photocorrosion [8]. Particularly ZnO nanostructures have been extensively studied as important wide-bandgap semiconductors (3.37 eV) [e.g. 9]. Carbon nanofibers (CNFs) possess unique physical and chemical properties and are widely used in nanoelectronics, sensing applications and in catalysis [10,11]. Recently, carbon nanofibers have been used as templates or scaffolds for assembly of various nanoparticles, such as Au–TiO_2, SiO_2–TiO_2, Ag, Pd or Ir–V, because of their hardness preserved even at high nanoparticle loadings [12–16]. The interest in using CNFs as catalytic support material arises due to their large surface area, high aspect ratio and their ability to disperse catalytically active particles [17]. Various techniques have been applied to obtain carbon nanofibers, such as chemical vapor deposition [18] or carbonizing electrospun precursors [19]. Electrospun precursors are usually obtained by the use of the PAN nanofibers [20]. Only a few works have employed TiO_2 or ZnO photocatalysts individually assembled on CNFs [21,22], and even less using their combinations. Several attempts have been made to reduce the recombination of photoinduced hole/electron pairs during the photocatalytic reactions by conjugation of the photocatalysts with electron scavenging agents such as metals, organic molecules or carbon nanofibers. Teng et al. introduced a novel $TiO_{2-x}N_x$/CNFs heterostructured photocatalyst [23]. In this work the authors proposed that owing to the synergistic effect of rather high adsorption capacity of CNFs and excellent vis-photocatalytic activity of $TiO_{2-x}N_x$ nanoparticles, the arrangement of the $TiO_{2-x}N_x$/CNFs showed higher photocatalytic efficiency than appropriate references of the TiO_2/CNFs and $TiO_{2-x}N_x$ [23].

The present work is a continuation of our recent studies on preparation, characterization and photocatalytic activity of different types of thin films [24–27].

2. Experimental

2.1. Preparation of layers

The films were initially prepared individually. All samples were deposited onto silicon wafers coated by a 100 nm thick titanium layer. The preparation of the CNFs was based on thermal calcinations of a polymer (polyacrylonitrile – PAN, Aldrich, average Mw 150,000) nanofibers web fabricated by the electrospinning proce-

* Corresponding author. Tel.: +420 266 052 198; fax: +420 286 581 448.
E-mail address: kment@fzu.cz (S. Kment).

0920-5861/$ – see front matter © 2010 Elsevier B.V. All rights reserved.
doi:10.1016/j.cattod.2010.10.001

dure. The homogenous clear solution was prepared by dissolving PAN and N,N-dimethylformamide at laboratory temperature. The polymer concentration was 15% (w/v). Conductivity of the solution was modified to 140 μS/cm by adding tetraethylammonium bromide. The prepared solution was placed into SPUR® noncommercial laboratory equipment working on the basis of needle electrospinning method. The flow rate was 2 ml/h, applied high voltage was 50 kV, electrode distance was 180 mm, temperature was 22 °C and relative air humidity was approximately 30%. The transformation of the as-deposited polymer web to the form of the CNFs was carried out under inert nitrogen atmosphere and using a thermal ramp. The temperature initially increased in the rate 5 °C/min up to 250 °C. At this temperature level the samples were stabilized for 30 min. Finally the temperature was increased with the same rate to 950 °C and left here for another two hours during which the carbonization was provided.

TiO_2 and ZnO thin layers were produced by means of a hollow cathode plasma jet system. The main advantage of this method lies in its capability to produce highly crystalline thin layers during the deposition procedure under certain precisely adjusted deposition conditions. It means that the temperature of substrates does not exceed 423 K when being coated and thus even thermally sensitive substrates (polymers) can be used. The system of two simultaneously working hollow cathode plasma jets was applied in the case of titanium dioxide thin films. The hollow cathodes are cooled titanium nozzles (purity 99.99%), which are connected to the DC pulsed supplier and also to the RF power supplier. The hollow cathodes were placed in the UHV chamber with marginal pressure of 10^{-6} Pa maintained by a turbomolecular pump. The real pressure level depends on the gases' flow rates and varies in the range of 2.5–5 Pa. Argon, flowing in each nozzle with the rate of 40 sccm ($cm^3\ s^{-1}$), serves as the working gas. The oxygen, fed to the chamber by a lateral entrance at a rate of 20 sccm, acts as the reacting gas. The first hollow cathode was placed perpendicular to the substrate and the angle between the nozzles was 30°. Between the supports positioned on a movable bench, and the hollow cathodes, a mask was situated in order to achieve thin films with high thickness homogeneity. The jets were connected to the supply of the DC pulse current with a frequency of 2.5 kHz and with an active discharge during 25% of the modulation period. Additionally, a low RF voltage with the power of 7 W was also used to increase the degree of ionization of the plasma. Grounded poles of static electromagnets were situated close to the nozzle outlet in order to provide a higher intensity and superior stability of the plasma stream in the reactor. DC pulsed hollow cathode discharge was broken down in the nozzle being sputtered due to ion bombardment. Argon gas flow was present in the sputtering nozzle. The sputtered particles were blown out of the nozzle into the reactor under the collateral oxidation and carried by this created plasma jet towards the substrate.

The ZnO layers were deposited using only one hollow cathode. The coating conditions were as follows: argon flow rate of 100 sccm, oxygen feeding of 10 sccm, RF power of 30 W and time of deposition of 2 h.

Characteristic photoelectrochemical features were evaluated and compared among a set of layers deposited by described methods. The individual tested layers and their compositions in hierarchical structures are coded in the text as: L1 – TiO_2 single thin films, L2 – TiO_2/CNFs, L3 – TiO_2/CNFs/ZnO and L4 – TiO_2/ZnO.

2.2. Characterization of layers

The crystallographic phases of the layers were determined with help of Raman spectroscopy. Unpolarized Raman spectra were recorded in a back-scattering configuration using Renishaw Raman Microscope RM 1000. The spectra were excited by the 514 nm Ar^+ line at a power <1 mW focused down to a spot of 2–3 μm in diameter. The spectral range was 150–4000 cm^{-1} and the resolution was ~1.5 cm^{-1}. The layers' morphologies and the formation of CNFs were studied by SEM Hitachi S-520 or Quanta 200. 3D surface pictures were also taken on the AFM microscope (Thericroscopes) and these were then analyzed to estimate the parameter of the relative surface roughness.

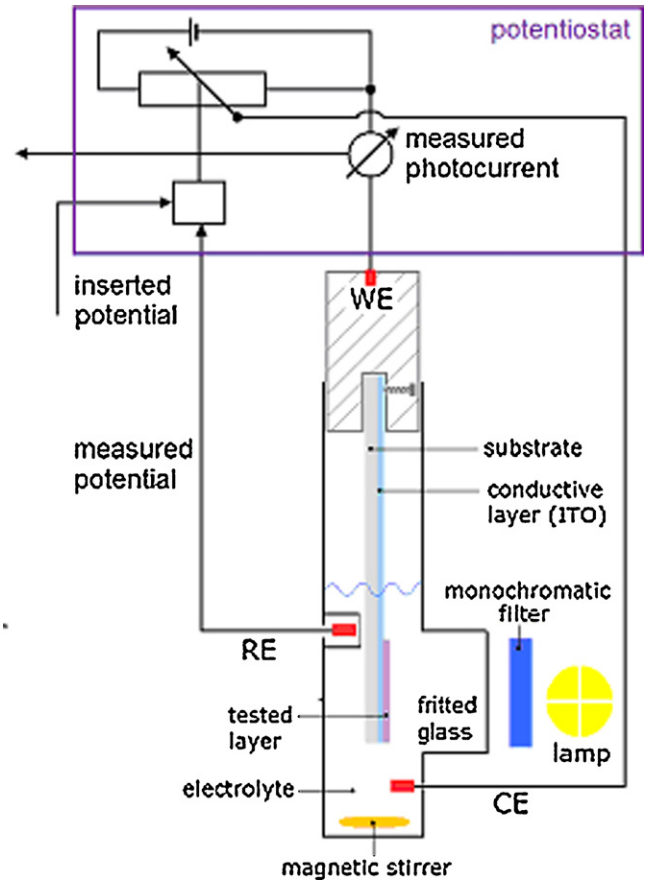

Fig. 1. Standard three-electrode photoelectrochemical arrangement. WE denotes working electrode, CE counter electrode and RE referential electrode.

2.3. Photoelectrochemical investigation of layers

The electrochemistry experiments were carried out using a three compartment electrochemical cell with three electrodes in the system (Fig. 1). The particular layer or the multilayer structure formed the working electrode (WE). As the referential electrode (RE), the Ag/AgCl electrode (environment of 3 M KCl) was employed and a platinum sheet introduced the counter electrode (CE). All these electrodes were immersed in the electrolyte solution (0.1 M Na_2SO_4). The layers were, during the experiments, illuminated by the polychromatic light from DC Arc polychromatic high pressure mercury lamp (LOT, LSH201/2 Hg, Xe) [28].

Three different kinds of measurements were performed. The dependency of current density on the applied potential to the tested layers – the polarization curves of the linear voltammetry were recorded in the periodic cycles of 5 s illumination (UV) of the layers and 5 s dark intervals. The experiments were run from the inserted potential of −400 mV to 1000 mV with the rate of the potential increase of 10 $mV\ s^{-1}$ with help of Voltalab PGZ-100 all-in-one potentiostat.

Such measurements expressing dependency of the current density on time with constant applied potential (600 mV – our

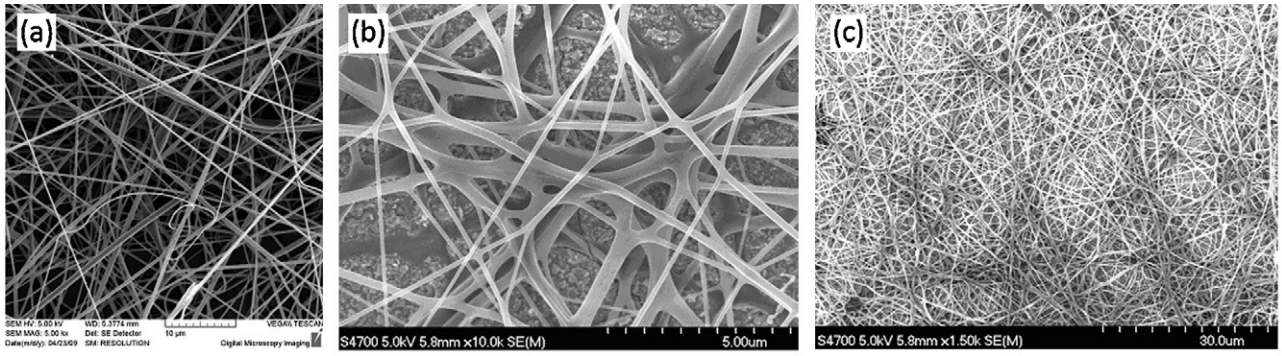

Fig. 2. SEM images of the nanofibers: (a) as deposited PAN nanofibers web, (b) carbonized PAN to the form of CNFs and (c) large area picture of CNFs.

conditions) are the basis of the amperometry. In this case, the light/dark period are extended up to one minute. In order to quantitatively compare the system, all the obtained photocurrent density data were recalculated according to Eq. (1) to the Incident-Photon-Current conversion Efficiency (IPCE) parameter, which is a commonly used quantum yield of a photoactivated reaction.

$$\mathrm{IPCE} = \frac{i}{\mathrm{FP}} \tag{1}$$

where i denotes the photocurrent density [A cm^{-2}], F is the Faraday constant (96.485 C mol^{-1}) and P the incident light intensity [Einsteins^{-1}].

Open circuit potential provides the information about the electron/hole pairs recombination kinetics. This measurement is again based on the combination of the dark/light periods. It is focused on monitoring changes of the potential over the total interval of 150 s. The procedure starts for 30 s in the dark. Then the shutter is opened and the working electrode irradiated for 60 s and finally the potential change is again monitored in the dark.

2.4. Photocatalysis – the surface wettability

To evaluate the surface wettability the surface contact angle is used. The measurements were performed on the See System 6.0 apparatus with a CCD camera and the mathematical evaluation software using the three point method for the circle circumscription.

3. Results and discussion

3.1. Characterization of layers

Fig. 2a shows the SEM image of the PAN nanofibers web prepared by the electrospinning method in the form of the thin layer. It is seen that the fibers are dispersed randomly but densely covering the whole substrate face. The thickness of the PAN web layer lies in the region between 100 and 150 nm. Surprisingly, the PAN web embodied a relatively high degree of adhesion to the substrate. The optimized annealing ramp carried out under nitrogen atmosphere yielded transformation of PAN nanofibers to the desired carbon nanofibrous form without losing their web structure

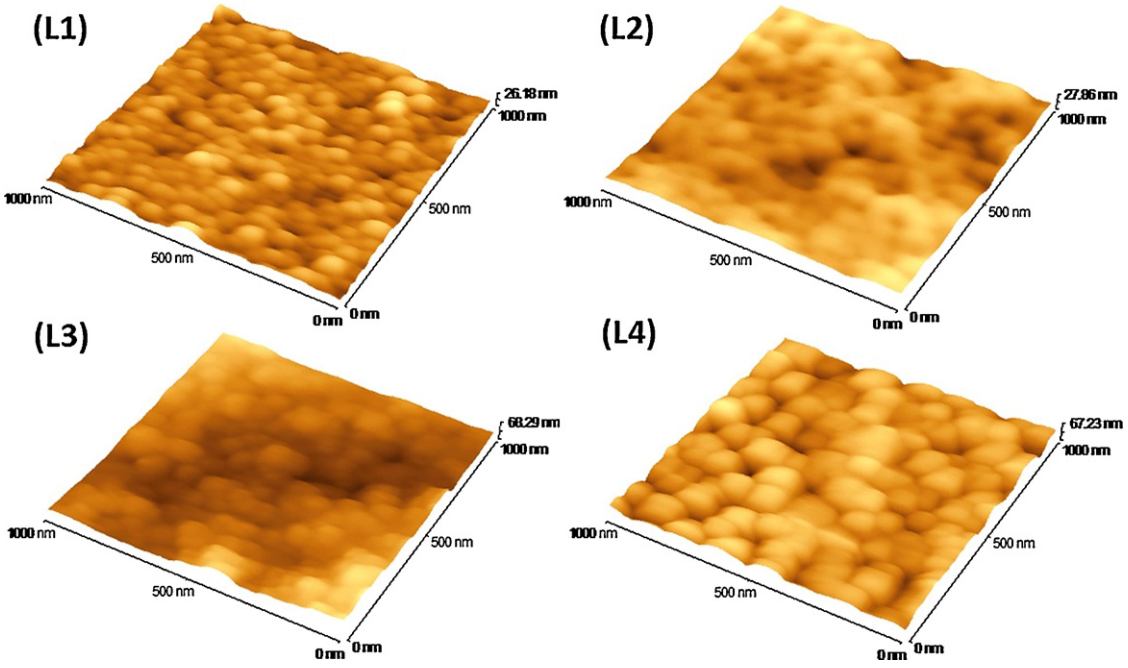

Fig. 3. Surface images of the system taken by AFM. The coding: L1 – TiO_2 single thin films, L2 – TiO_2/CNFs, L3 – TiO_2/CNFs/ZnO and L4 – TiO_2/ZnO.

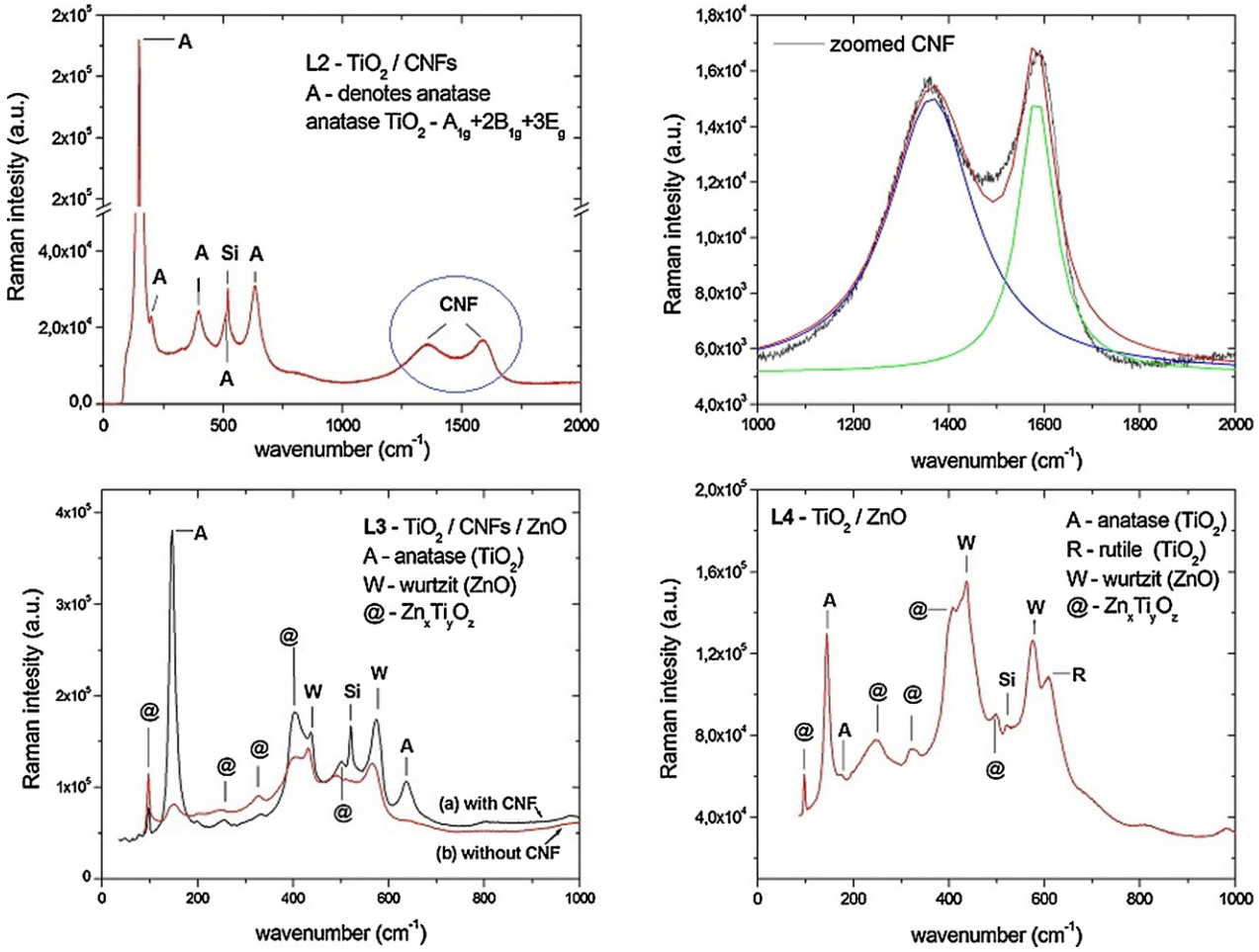

Fig. 4. The Raman spectra of the prepared arrangements.

(Fig. 2b). Moreover, the thermal procedure also improved the adhesion to the substrate, which together with their sufficient hardness enabled easy manipulation of the samples (CNFs' area is depicted in Fig. 2c).

Morphologies of heterostructures were visualized with help of AFM (Fig. 3) together with the assessment of the relative roughness of the layers (rms parameter). The morphology of the system L2 (CNFs/TiO_2) was not influenced by the carbon fibers. The TiO_2 layer covering the CNFs was compact and very similar in its morphology to the TiO_2 layer deposited individually (in Fig. 3 compare L1 and L2). The relative roughness of these layers was also very close (L1 rms – 3.52 nm; L2 rms – 4.72 nm). An increase of layers' roughness was observed when ZnO films were coated onto TiO_2. The rms values were determined as 12.4 nm and 9.9 nm for L3 and L4 respectively. On the other hand, every system embodied sufficient homogeneity without defects and relatively high smoothness.

Crystallographic structures of created systems were judged by Raman spectroscopy. The Raman spectra of the layers L2, L3, L4 are available in Fig. 4. The L1 spectrum is missing due to the spectral identity of TiO_2 layers in assembly types L1 and L2. All the intensive Raman peaks (bends) located at frequencies 143, 196, 395, 513, 519 and 638 cm^{-1}, which are attributed to the anatase tetragonal structure TiO_2 [29], can be assigned in spectra of L2 (Fig. 4). The bends correspond to six active Raman modes of representations $A_{1g} + 2B_{1g} + 3E_g$, which relate to the space group D_{19}^{4h} ($I4/amd$). In the L2 spectrum there are also two broad bends positioned at 1356 and 1586 cm^{-1} corresponding to the D and G bands of a bundle of carbonized fibers. Generally, the D band is related to the disordered turbostatic structures whereas the G band is related to the ordered graphitic structures. The ratio between integrated relative intensity of the D band peak and G band peak is termed as R-value and it expresses the degree of representation of structurally ordered graphite crystallites in carbonaceous materials [20,30]. As expected in the case of L2, $R = 0.94 \pm 0.04$, which means that the layers are formed more by disordered carbon structure. Very interesting Raman spectra having important informative character in terms of the photocatalytic activity of the systems TiO_2–ZnO were obtained from L3 and L4 samples. In the case of the type L3, the Raman spectra were recorded at the point of coexistence of all the present layers (TiO_2, CNFs, ZnO) and those without CNFs. The peaks related to anatase TiO_2 (143 and 638 cm^{-1}) and wurtzite ZnO (437 and 636 cm^{-1}) can be clearly distinguished when the spectra were taken out of the CNF position. Unexpected remaining peaks (~98, 250, 320, 400 and 500 cm^{-1}) can probably be assigned to various ZnO–TiO_2 mixture structures in the forms of $Zn_xTi_yO_z$ (a mixture of e.g. spinel type Zn_2TiO_4 – cubic, $ZnTiO_3$ – hexagonal, $Zn_2Ti_3O_8$ – cubic). It has been shown above that the pure anatase TiO_2 structure was primarily obtained (Fig. 4, L2). The plasma is a very energetic environment, and obviously, during the ZnO films deposition, the plasma activated zinc ions interacted with the TiO_2 layer yielding also the $Zn_xTi_yO_z$ structure besides the demanded wurtzite ZnO layer [31,32]. In relation to photocatalysis, it is important to notice the remarkable decrease of the anatase TiO_2 phase (photocatalytically the most active phase) at the point of TiO_2 + CNF coexistence where the $Zn_xTi_yO_z$ growth probably predominated. Moreover, the

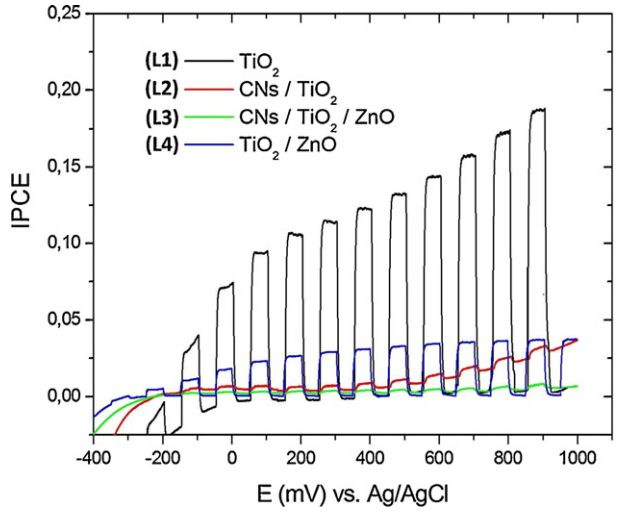

Fig. 5. Polarization curves of the linear voltammetry. UV light with the maximum at 365 nm. Incident light intensity $P = 3.415 \times 10^{-4}$ Einstein s^{-1} cm^{-2}.

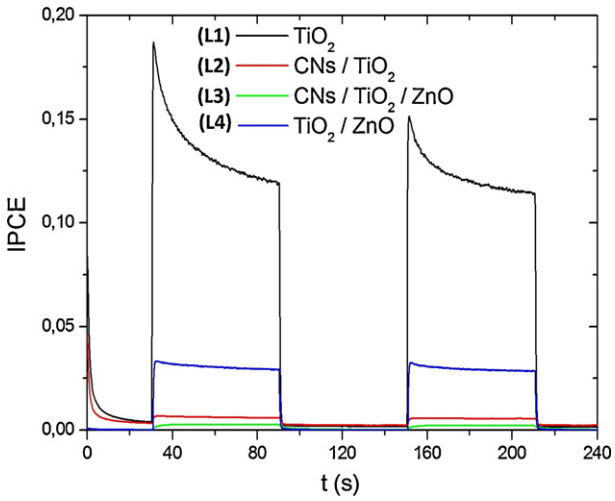

Fig. 6. Amperometry of the samples. UV light with the maximum at 365 nm. Incident light intensity $P = 3.415 \times 10^{-4}$ Einstein s^{-1} cm^{-2}.

Raman band at 612 cm^{-1}, which relates to the rutile form of TiO_2, was determined for L4.

3.2. Photoelectrochemistry of the layers

Polarization curves shown in Fig. 5 express the ability of layers to produce a measurable photocurrent while being illuminated by light with the appropriate wavelength. This phenomenon is associated with the photocatalytic process already described in the introduction. Moreover, it is well known that the photocatalytic activity can be improved by applying external voltage to the photocatalyst due to the efficient separation of photogenerated species (negative electrons and positive holes). Surprisingly, the highest photoelectrochemical response was observed in case of individual TiO_2 thin films, which was entirely opposite to the assumption. It was expected that the generated electrons would be effectively drawn away from the activated TiO_2 particle preventing the electrons/holes backwards recombination, which is the most limiting aspect of the photocatalysis. It was already pointed out that the principle of plasma deposition is based on the reaction of highly activated species in the plasma environment. In the context of this research, it is suggested that an unexpected process probably took place. Applying the plasma deposition for TiO_2 covering the CNFs led to the contaminations of TiO_2 particles by the carbon atoms being sputtered from CNFs. Such impurities apparently created the "new" states in the TiO_2 band gap capturing the photoexcited electrons. As a result, the significant decrease of photocurrents in the case of L2 is observed (Fig. 5). The relatively low values of photocurrents are also seen graphically for remaining types of systems (L3 and L4). This is apparently the consequence of the grown $Zn_xTi_yO_z$ structure inhibiting the photoelectrochemical process and also the observed decrease of anatase phase of TiO_2.

The amperometry measurements were aimed to provide information about the time stability of the photocatalysts. Obviously the results reflect the previous discussion (Fig. 6). However, it is important to notice that only the L1 type embodied the so called current peak, which can be seen as the very sharp maximum of IPCE at the point when the light is on. Further, the IPCE decrease constantly to a certain steady state value. The immediate IPCE increase means a rapid electrons/holes separation. In our previous work, it was established and approved that the current peak is missing for such doped TiO_2 layers, in which the dopant produces the electron traps in the forbidden band of TiO_2 particles [33]. This underlines the assumption that the photocatalytic activity is reduced due to the carbon doping of TiO_2.

The measurement of the open circuit potential (E_{oc}) is a powerful photoelectrochemical method for the quantification of the positive holes present on the surface of the tested layer. Fig. 7 represents the trend of the open circuit potential curves as dependency on time. Generally, the higher the potential value, the higher amount of reacting holes. Very different behavior of the systems is seen in Fig. 7. Contrary to the preceding results, the systems including ZnO thin layers (L3 and L4) quoted indispensable improvement in their photoresponses. The decrease of the E_{oc} reflects electric charge transferred onto the surface of the semiconductor. It is a consequence of the fact that photogenerated holes react fast on the surface leading to the access of the electrons, which therefore accumulate on the TiO_2 surface and charge it negatively. In terms of good photoelectrochemical properties of TiO_2 and its various arrangements, the undisturbed electrons flow is the most important. Whereas in the case of the photocatalysis, to create a high amount of holes with efficient life time is in the highest interest. Both these requirements are reflected in the necessity to avoid the fast electrons/holes backward recombination. However, considering that the decrease of the E_{oc} quantifies the amount of the holes

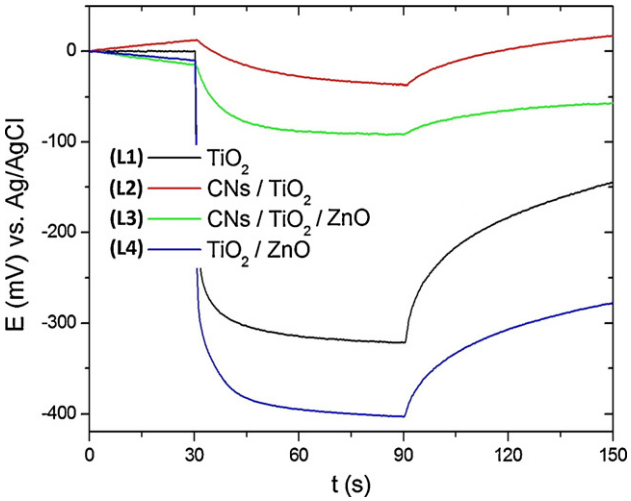

Fig. 7. Open circuit potential trends. UV light with the maximum at 365 nm. Incident light intensity $P = 3.415 \times 10^{-4}$ Einstein s^{-1} cm^{-2}.

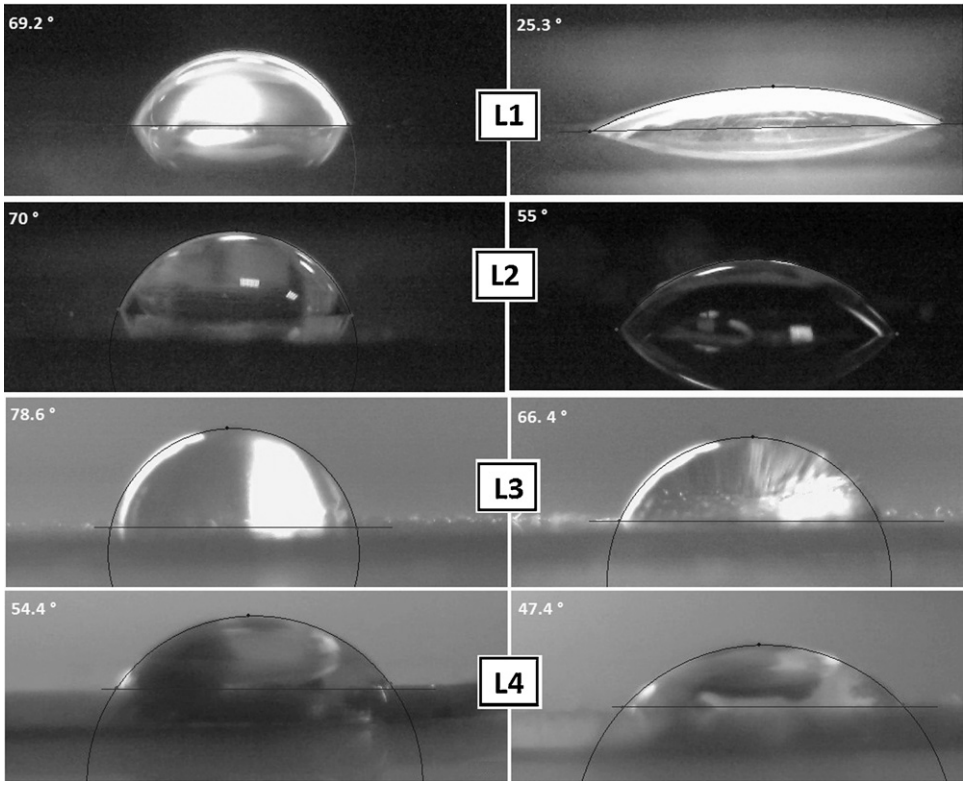

Fig. 8. Photocatalytic activity of the systems expressed as the water surface wettability – the measurements of the surface contact angles. The left column – before UV irradiation and the right column – after 1 h UV irradiation.

at the surface of the particle and hence the photocatalytic activity. It could be concluded that the low photoelectrochemical response does not necessarily mean the low photocatalytic activity. In other words, whereas the L3 and L4 systems were qualified as the poor photoelectrochemical agents due to the presence of the electron traps, they still might be referred as the photocatalysts with certain activity. The deeper studies devoted to the correlation between the E_{oc} and the photocatalytic activity have been reported elsewhere [34,35].

3.3. Photocatalytic activity of the systems

The photocatalytic activities of the systems were determined using a simple test based on the contact angle evaluation (surface wettability). The experiments lied in the measurements of the contact angles before and after irradiation of the studied layers/composites. Basically, due to UV irradiation of TiO_2, highly oxidative species (hydroxyl groups) are generated at its surface. These species react with the impurities adsorbed on the TiO_2 surface creating the "super clean" surface, and therefore, the contact angle of a water droplet is being reduced. Moreover, the hydroxyl groups serve as metastables, which even enhance the hydrophilicity of the TiO_2 surface. The higher the photocatalytic activity the lesser the contact angle. All of the tested system revealed certain decrease of the contact angle (see Fig. 8). In agreement to the photoelectrochemical experiments the highest photocatalytic activity was seen in case of the bare TiO_2 films.

4. Conclusion

In this contribution the photoelectrochemical functionality of the multilayer system consisting of CNFs/photoactive anatase TiO_2/conductive ZnO thin films has been discussed. The CNFs in the form of thin layers were prepared by thermal carbonization of the polymer PAN nanofibers web. The webs were fabricated by means of SPUR® equipment based on the principle of electrospinning deposition method. Individual crystalline thin films of anatase TiO_2 and wurtzite ZnO were coated using low temperature plasma hollow cathode method. The high crystalline films were produced under the very low temperature of the substrate (below 420 K). However, it was shown that the high energy of Ti and Zn atoms led to the formation of carbon doped (from CNFs) TiO_2 and $Zn_xTi_yO_z$ respectively when the multilayer system was being prepared. This phenomenon crucially influenced both photoelectrochemical and photocatalytic responses of the systems. In other words, the highest photocurrent values were achieved for isolated TiO_2 thin films. On the other hand, it was shown that although the systems including ZnO layers as one of constituents embodied the lowest photoelectrochemical activity, they still could be used as the active photocatalysts.

Acknowledgements

The authors wish to acknowledge the Grant Agency of Academy of Sciences of the Czech Republic (projects – KAN400720701 and KAN301370701) and the Ministry of Education of the Czech Republic (projects – Nanopin 1M0577 and 1M06002).

References

[1] J.A. Navio, C. Cerrillos, M.A. Pradera, E. Morales, J.L. Gomez-Ariza, Langmuir 14 (1998) 388–395.
[2] C.P. Chang, J.N. Chen, M.C. Lu, H.Y. Yang, Chemosphere 58 (2005) 1071–1078.
[3] B. O'Regan, M. Gratzel, Nature 353 (1991) 737–740.
[4] M. Gratzel, Nature 414 (2001) 338–344.
[5] Z. Zhang, Y. Yuan, Y. Fang, L. Liang, H. Ding, L. Jin, Talanta 73 (2007) 523–528.
[6] K. Fujishima, Honda, Nature 238 (1978) 37.
[7] J. Chen, M. Yao, X. Wang, J. Nanoparticle Res. 10 (2008) 163–171.
[8] C. Ye, Y. Bando, G. Shen, D. Golberg, J. Phys. Chem. B 110 (2006) 15146–15151.
[9] L.S. Mende, J.L. MacManus-Driscoll, Mater. Today 10 (2007) 40–48.

[10] X.F. Tang, Y. Liu, H.Q. Hou, T.Y. Tou, Talanta 80 (2010) 2182–2186.
[11] P.W.A.M. Wenmakers, J. van der Schaaf, B.F.M. Kuster, J.C. Schouten, Chem. Eng. Sci. 65 (2010) 247–254.
[12] H.J. Zhang, J.S. Huang, H.Q. Hou, T.Y. You, Electroanalysis 21 (2009) 1869–1874.
[13] P.C.P. Watts, S.J. Henley, E. Mendoza, S.R.P. Silva, J.K. Irvine, E.T. McAdams, Nanotechnology 18 (2007) 205502.
[14] N. Hammer, I. Kvande, X. Xu, V. Gunnarsson, B. Totdal, D. Chen, M. Ronning, Catal. Today 123 (2007) 245–256.
[15] B.H. Kim, S.K. Nataraj, K.S. Yang, H.G. Woo, J. Nanosci. Nanotechnol. 10 (2010) 3331–3335.
[16] J.S. Zheng, X.Z. Wang, J.L. Qiao, D.J. Yang, B. Li, P. Li, H. Iv, J.X. Ma, Electrochem. Commun. 12 (2010) 27–31.
[17] N. Keller, G. Rebmann, E. Barraud, O. Zahraa, V. Keller, Catal. Today 101 (2005) 323–329.
[18] S.S. Kim, K.W. Kim, H.J. Ahn, K.K. Cho, J. Alloys Compd. 449 (2008) 274–278.
[19] A.A. Ali, G.C. Rutledge, J. Mater. Process. Technol. 209 (2009) 4617–4620.
[20] E. Zussman, X. Chen, W. Ding, L. Calabri, D.A. Dikin, J.P. Quintana, R.S. Ruoff, Carbon 43 (2005) 2175–2185.
[21] Y. Hong, D. Li, J. Zheng, G. Zou, Nanotechnology 17 (2006) 1986–1993.
[22] D.F. Shao, Q.F. Wei, L.W. Zhang, Y.B. Cai, S.D. Jiang, Appl. Surf. Sci. 254 (2008) 6543–6546.
[23] D.H. Teng, Y.H. Yu, H.Y. Liu, X.P. Yang, S. Ryu, Y.H. Liu, Catal. Commun. 10 (2009) 442–446.
[24] S. Kment, P. Kluson, H. Bartkova, J. Krysa, O. Churpita, M. Cada, P. Virostko, M. Kohout, Z. Hubicka, Surf. Coat. Technol. 202 (2008) 2379–2383.
[25] S. Kment, P. Kluson, V. Stranak, P. Virostko, J. Krysa, M. Cada, J. Pracharova, M. Kohout, M. Morozova, P. Adamek, Z. Hubicka, Electrochim. Acta 54 (2009) 3352–3359.
[26] S. Kment, P. Kluson, Z. Hubicka, J. Krysa, M. Cada, I. Gregora, A. Deyneka, Z. Remes, H. Zabova, L. Jastrabik, Electrochim. Acta 55 (2010) 1548–1556.
[27] S. Kment, P. Kluson, H. Zabova, A. Churpita, M. Chichina, M. Cada, I. Gregora, J. Krysa, Z. Hubicka, Surf. Coat. Technol. 204 (2009) 667–675.
[28] G. Waldner, M. Purmodjib, R. Bauer, M. Neuman-Spallart, Chemosphere 50 (2003) 289–298.
[29] T. Ohsaka, F. Izumi, Y. Fujiki, J. Raman Spectrosc. 7 (1978) 321–324.
[30] Z. Zhou, Ch. Lai, L. Zhang, Y. Qian, H. Hou, D.H. Reneker, H. Fong, Polymer 50 (2009) 2999–3006.
[31] S. Sedpho, D. Wongratanaphisan, P. Mangkorntong, N. Mangkorntong, S. Choopun, J. Nat. Sci. 7 (2008) 99–104.
[32] L. Hou, Y.D. Hou, M.K. Zhu, J. Tang, J.B. Liu, H. Wang, H. Yan, Mater. Lett. 59 (2005) 197–200.
[33] S. Kment, H. Kmentova, P. Kluson, J. Krysa, Z. Hubicka, V. Cirkva, I. Gregora, O. Solcova, L. Jastrabik, J. Colloid Int. Sci. 348 (2010) 198–205.
[34] K.J. Zhang, W. Xu, X.J. Li, S.J. Zheng, G. Xu, Cent. Eur. J. Chem. 4 (2006) 234–245.
[35] J. Krysa, J. Jirkovsky, J. Appl. Electrochem. 32 (2002) 591–596.